

## **Detachment stabilization with $n/m=1/1$ resonant magnetic perturbation field applied to the stochastic magnetic boundary of the Large Helical Device**

M. Kobayashi, S. Masuzaki, I. Yamada, N. Tamura, Y. Feng\*, K. Sato, M. Goto, Y. Narushima, T. Akiyama, J. Miyazawa, M. Shoji, S. Morita, B.J. Peterson, H. Funaba, N. Ohyabu, K. Narihara, T. Morisaki, H. Yamada, A. Komori, the LHD experimental group and D. Reiter\*\*

*National Institute for Fusion Science, Oroshi-cho 322-6, Toki city, Gifu 509-5292, Japan*

*\*Max-Planck-Institut für Plasmaphysik, EURATOM-IPP Association D-17491, Greifswald, Germany*

*\*\*Institut fuer Plasmaphysik, Forschungszentrum Juelich GmbH, D-52425 Juelich, Germany*

### Abstract

It is found that the remnant island structure created by  $n/m=1/1$  resonant magnetic perturbation field in the stochastic magnetic boundary of the Large Helical Device (LHD) [A. Komori et al., Nucl. Fusion **49**, 104015 (2009).] has a stabilizing effect on formation of radiating plasma, realizing stably sustained divertor detachment operation with the core plasma being unaffected. The data from the several diagnostics, (profiles of electron temperature & density, radiation and temporal evolution of divertor particle flux) indicate selective cooling around X-point of the island and thus peaked radiation there, which is stabilized outside of the last closed flux surface throughout the detachment phase. The VUV spectroscopy measurements of high Z impurity (iron) emission shows significant decrease during the detachment, indicating core plasma decontamination. The results from the 3D edge transport code EMC3 (Edge Monte-Carlo 3D) [Y. Feng et al., Contributions to Plasma Physics, **44**, 57 (2004).]-EIRENE [D. Reiter et al., Fusion Sci. Technol., **47** 172 (2005).] show similar tendency in the radiation pattern. The island size and its radial location are varied to investigate the magnetic topology effects on the detachment control. The divertor particle flux and neutral pressure exhibit intermittent oscillation as well as modification of recycling pattern during the detachment, which are found to reflect the island structure.

## I. INTRODUCTION

Numerous experiments in various devices have demonstrated that the detached divertor plasma can be an option for divertor operation in future devices in order to reduce the peak power load at the target plates below the engineering limit [1,2,3,4]. However, control of the detached divertor plasma still remains one of the most challenging issues for magnetically confined devices because of its complex mechanism of the plasma detachment from target plates as well as of the location of radiation, where the strongly nonlinear temperature dependence of atomic-molecular process at the cold plasma, energy transport parallel & perpendicular to magnetic field and thus its flux tube geometry, play important roles. As has been observed in the X-point divertor tokamaks often at the relatively higher density above the detachment transition, the radiation region proceeds along the temperature gradient parallel to the magnetic field, and it is usually found to be “stabilized” around the X-point of the divertor configuration, forming radiative condensation with extremely dense ( $> 10^{20} \text{ m}^{-3}$ ) and cold (a few eV) plasma [5,6,7,8,9]. The phenomena are called X-point MARFE (Multifaceted Asymmetric Radiation From the Edge) and often lead to confinement degradation [6,9]. The geometrical feature of the X-point, i.e. very small field line pitch as well as the flux expansion around X-point are considered to be one of the reasons for the formation of X-point MARFE, although the analysis is still ongoing and the mechanism is not yet fully understood.

On the other hand, the helical devices, e.g. the Large Helical Device (LHD) [10] and Wendelstein7-AS (W7-AS) [11] etc have large flexibilities of changing the magnetic field structure in the edge region by controlling the current distribution in main/perturbation coils, i.e. location and number of magnetic island chains/X-point. This provides us possibilities to investigate geometrical effects on the detachment stability. In LHD, the analyses on radiation pattern during the radiative collapse phase [12] as well as on operational space of detachment realization [13] were performed. However, systematic study concerning the magnetic field structure has not yet been done. In W7-AS, which has island divertor configuration, it was found that the island size and the field line pitch inside the islands influences the detachment stability [14, 15].

In this paper, we report the dedicated experiments to investigate the geometrical effects of edge magnetic structure on the detachment stability in LHD, utilizing  $n/m=1/1$  resonant magnetic perturbation field applied to the stochastic magnetic boundary. The  $n/m=1/1$  remnant island seems to have stabilizing effect on the radiation region, and the detachment phase was sustained until the end of discharge that was terminated by stop of NBI heating. It is observed that the divertor power load estimated by the divertor probe was significantly reduced, and that the stored energy in the plasma was kept constant during the detachment or even slightly improved compared with those in the attached phase. Without the island, density ramp up simply leads to radiative collapse as soon as the plasma detaches the divertor plates overriding the feed-back gas puff control. This difference indicates importance of the field line geometry for the stability of detachment. The size of the island

and its radial location were varied in order to study the geometrical effects on the detachment stability. The numerical analysis with the 3D edge transport code, EMC3 [16]-EIRENE [17], was performed to interpret the experimental results.

Although the underlying mechanism of the stabilization of the detachment phase with the  $n/m=1/1$  perturbation field is under investigation, these experimental data including those of W7-AS indicate a possibility to establish a scheme to control detachment in future devices utilizing the flexibility of the three dimensional divertor configuration, not only in helical devices but also in the non-axisymmetric tokamaks with the resonant magnetic perturbation field such as Tore Supra [18], Tokamak Experiment for Technology Oriented Research - Dynamic Ergodic Divertor (TEXTOR-DED) [19], Doublet III-D (DIII-D) [20] and Joint European Torus (JET) [21] etc.

In the next section, the magnetic field structure of the LHD edge region is explained. In the section III, the typical controlled detachment discharge is presented. The radiation pattern during the detachment is investigated in the section IV using several diagnostics and the numerical simulation with EMC3-EIRENE. In section V, effects of the island size and the radial location on the detachment control are discussed. The section VI gives the detailed observation of the divertor flux change during the detachment as a signature of modification of recycling pattern. The paper is summarized in the section VII.

## II. MAGNETIC FIELD STRUCTURE

The Large Helical Device (LHD) is a heliotron type device as shown in Fig.1. The magnetic field is produced by the superconducting coils with poloidal winding number of  $l = 2$  and toroidal field periods of  $n = 10$  [22]. The major radius and the averaged minor radius of plasma (including the scrape off layers, SOL) are 3.9 m and 0.7 m, respectively. Because of the mode spectrum of magnetic field produced by the helical coils, the magnetic islands of different mode numbers are created, and they overlap each others. It has, therefore, intrinsically a stochastic field line structure in the edge region. Fig.2 (a) shows the connection length distribution at the edge of LHD, with different colors representing different connection lengths, e.g. dark blue for  $\sim 1$  m and bright yellow for  $> 10$  km. The stochastic field lines are characterized by the long connection length of  $> 100$  m as shown in the figure, while there exist also remnant islands due to incompleteness of the overlapping, which appear as white spots indicating infinite connection length inside the remnant islands. The region consisting of the long connection field lines with the remnant islands are called the stochastic region [22]. The outer most region is characterized with mixture of long and short connection lengths. This structure is created by the remnant islands which are stretched beyond the X-point and cut by the divertor plate, where the field lines inside the islands connect the plate to plate with rather short length due to the regular motion of field lines, while those around separatrix travel long

distance because of the singularity and the stochastization there. As a result, the mode structure in this region has short connection length field lines surrounded by the long ones. This outer most region is called edge surface layers [22], which is the similar structure as also found in other devices like Tore Supra [23] and TEXTOR-DED [19] where it is called laminar region.

The  $n/m=1/1$  resonant magnetic perturbation field is applied by the coils installed at the top and bottom of the machine as shown in Fig.1 (a) in order to create a magnetic island in the stochastic region. Fig.2 (b) shows the connection length distribution with the perturbation field, where the O-point of remnant island of  $n/m=1/1$  mode is found at the outboard side with white color indicating infinite connection length inside island. Since the island is embedded in the stochastic region, the separatrix is no longer clear. The X-point of the island is, therefore, not visible in the plot. By strict definition, it may not be called so. In the following, however, we may keep the term “X-point” representing the region where a clear X-point would have existed without the stochastization, or just poloidally opposite side to the O-point.

### III. DETACHMENT SUSTANMENT WITH $N/M=1/1$ ISLAND

Figure 3 shows the time traces of plasma parameters obtained in the sustained detachment shot with the  $n/m=1/1$  perturbation field (shot number : 85946). The discharge was initiated at  $t=1.3$  s by the neutral beam injection (NBI) heating, and the density was ramped up by gas puff gradually. The divertor particle flux (ion saturation current, Fig.3 (b)) measured by the Langmuir probe arrays, as a sum of all probe tips, increases linearly with respect to the density rise until the detachment transition without exhibiting high recycling regime that is characterized with the square scaling as observed in X-point poloidal divertor tokamaks. Also the  $n_e$  and  $T_e$  at the divertor plates show rather modest change against the density scan, which has been also reported in ref.[24]. The absence of the high recycling regime has been interpreted as being due to the parallel momentum loss in the stochastic SOL as discussed in ref.[25, 26, 27]. Around  $t=2.9$  s with the line averaged density of about  $6 \times 10^{19} \text{ m}^{-3}$ , the divertor particle flux decreased by a factor of 3 and the divertor heat flux (Fig.3 (d)) estimated by the probes dropped by a factor of 3 ~ 10, showing detachment transition. The large scatter during detachment is due to the difficulty in obtaining probe characteristics at the low temperature plasma and also caused by intermittent divertor flux oscillation discussed in detail in section VI. The divertor plasma temperature at the detachment transition was estimated at slightly above 5 eV and during the detachment it is estimated around 5 eV but with error bars of order of several eV. At the transition, the radiation intensity measured by AXUVD (Absolute eXtreme Ultra Violet photoDiode) array, which detects the radiation of energy range from 1.1 eV to 6000 eV (wave length of 0.04 ~ 1100 nm), increases by a factor of about 3, which is roughly consistent with the decrease in the divertor power flux within the error bars of measurements. The line ratio of hydrogen

emission  $H_\gamma/H_\beta$  measured by the visible spectroscopy shows increase at the almost all toroidal sections as shown in Fig.3 (h), indicating the presence of volume recombination throughout the torus, while  $H_\alpha$  stays at slightly increased level during the detachment (Fig.3 (e)). The residual particle flux of about 10~30% is due to the remaining flux in the private region while the peak value at the strike point decreases by about one order of magnitude as shown later in section VI and Fig. 13. Even after the transition, the density continued to increase slowly for  $\sim 0.6$  seconds, and finally reached a steady state at  $9 \times 10^{19} \text{ m}^{-3}$ . The gas puff rate which is controlled by a feedback system was decreased indicating increase of particle confinement time during the detachment. The detachment phase was sustained up to the end of discharge which was terminated by stop of NBI. No confinement degradation was observed as shown in the stored energy ( $W_p$ ) time trace in Fig.3 (f) or it is even slightly increased after the detachment transition. This improvement of the stored energy is distinct feature from the previous detachment operation [13]. The difference might come from the location of radiation region, which is inside the last closed flux surface (LCFS) in the magnetic configuration (magnetic axis  $R_{ax}=3.60$  m) of [13] and while it is outside LCFS in the present configuration ( $R_{ax}=3.90$  m) as discussed later in Fig.7 as well as in Fig.8 in section IV. Plotted in fig.4 are radial profiles of electron temperature ( $T_e$ ), density ( $n_e$ ) and the pressure ( $T_e n_e$ ) before and after the detachment transition at  $t=2.8$  and  $4.0$  s, respectively.  $T_e$  was slightly decreased in the detachment phase while  $n_e$  increased by a factor of 2. The resultant pressure profile increased after the detachment transition with steeper gradient at the edge region. This is consistent with the increase in  $W_p$  obtained by the diamagnetic measurement. It is also seen that around  $R=4.75$  m there appears large peak in the density profile, even larger than the central density. This is considered due to the cool down of the outer most region due to the carbon radiation as discussed later.

As seen in the well maintained stored energy level during the detachment phase, one expects no impurity contamination during the detachment. This is confirmed with the VUV spectroscopy measurement of iron emission spectra as plotted in Fig.5 for different densities. At the rather low density with attached plasma at  $2.0 \times 10^{19} \text{ m}^{-3}$ , there appears clear line emissions from the low to high charge states of iron, Fe VIII ~ XXIII, which are coming from the sputtered iron from the first wall made of stainless steel. At the high density operation with attached plasma of  $4.0 \times 10^{19} \text{ m}^{-3}$ , the most of the lines are significantly suppressed. The effect is considered due to the impurity screening of the stochastic magnetic field at the high density operation as discussed in ref.[28, 29, 30]. The reduction of the emission from the low charge states might also be attributed to the reduction of iron source due to the dense and cold edge plasma which shifts the energy spectrum of charge exchange flux to the first wall to lower energy range with which the iron is hardly sputtered. It is important to note that this screening effect is available during the detachment phase as shown in the Fig.5, keeping the core plasma free from impurity contamination.

In the case without the  $n/m=1/1$  island, it is difficult to sustain the detached plasma and usually

it leads to radiative collapse, as shown in Fig.6, where the time traces of line averaged density, radiation intensity measured by AXUVD, and the ion saturation currents are plotted. The density reaches  $6.0 \times 10^{19} \text{ m}^{-3}$  around  $t=2.6 \text{ s}$ , and the ion saturation current saturates. At  $t = 3.9 \text{ s}$  the ion saturation current starts to decrease, but the density can no longer be controlled by the feed-back gas puff and the plasma goes to radiative collapse.

Clear differences between the both cases are found in the edge plasma parameter profiles,  $T_e$  and  $n_e$ , obtained with the Thomson scattering system at the outboard mid-plane as plotted in Fig.7. In the case without the island (Fig.7 (a), (b)), the  $T_e$  monotonically decreases at the entire edge region as the density is raised, and finally the plasma goes to radiative collapse at the loss of density control. In the case with the island (Fig.7 (c), (d)), on the other hand,  $T_e$  continuously decreases with increasing density at the outer most region,  $R > 4.75 \text{ m}$ , until the detachment transition. But after the transition, it is stabilized around a few eV, while keeping almost same  $T_e$  at the inner region  $R \sim 4.55 \text{ m}$  throughout the density rise. In-between the inner and outer most regions there appears flattening of  $T_e$  caused by the magnetic island flux tubes, where  $T_e$  is kept at more than 10 eV due to the strong parallel transport even at the detachment phase. Assuming coronal equilibrium for the carbon radiative power loss rate coefficient,  $L(T_e)$ , which has maximum value at  $5 \sim 7 \text{ eV}$ , the radiation intensity,  $Cn_e^2 L(T_e)$  with  $C$  being carbon concentration, is expected to be peaked around  $R = 4.74 \text{ m}$ , which corresponds to the peak of  $n_e$  as well with  $\sim 10^{20} \text{ m}^{-3}$ . During the detachment phase, this  $T_e$  and  $n_e$  profiles are sustained with the feed-back control of gas puff. It is noted that this flux tube around  $R = 4.74 \text{ m}$  that expected to radiate strongly is far outside of LCFS with the confinement region being untouched by the impurity radiation. It looks like that the robust  $T_e$  flattening inside the island prevents the radiation region from penetrating inward. The experimental evidence of the effects on the radiation distribution is shown in the next section.

#### IV. RADIATION PATTERN DURING THE DETACHMENT

As discussed with the edge  $T_e$  profiles in the previous section, the  $n/m=1/1$  island can modify the radiation pattern by introducing modulation of  $T_e$  distribution such as flattening inside the island. Significant differences are observed in the radiation pattern during detachment. Plotted in Fig.8 (a) are the line integrated radiation profiles measured by the AXUVD for without (left) & with (right) the island, respectively. The viewing lines of the each photo diode are indicated in Fig.8 (b) as well. In the case of radiative collapse without the island (Fig.8 (a) left), the radiation profile is broad over the almost all channels at high density ( $t > 2.5 \text{ s}$ ) until the plasma goes to radiative collapse at  $t=4.0 \text{ s}$ , while in the sustained detachment (Fig.8(a) right) strong asymmetry is observed, i.e. there appears a strong peak after the detachment transition around ch.4 which passes through the bottom part of the plasma cross section, and the peak is kept throughout the detachment phase. In this cross section, the

O-point of the  $n/m=1/1$  island is located at the top of plasma, so that the bottom part of the plasma corresponds to the X-point. The edge plasma transport simulation with EMC3-EIRENE is being conducted. EMC3 solves the Braginskii type fluid equations of mass, momentum and energy in 3D magnetic field/plasma facing components geometry [16]. The code is coupled with EIRENE [17] which solves kinetic neutral transport equations to incorporate the recycling neutrals from divertor plates and the first wall. The impurity radiation distribution obtained from the computation with the density at the LCFS ( $n_{LCFS}$ ) of  $7.0 \times 10^{19}$  and  $6.5 \times 10^{19} \text{ m}^{-3}$  are plotted in Fig.8 (c) for without (left) & with (right) the island, respectively. The selected  $n_{LCFS}$ 's correspond to  $t \sim 3.0$  and  $3.1$  s for without and with island. Since the density continues to increase in the case of island at  $t \sim 3.1$  s as shown in Fig.3 (a), the further increase of density in the computation is ongoing, which is not yet converged and will be reported in a separated paper. In the case without the island (left figure) the maximum radiation intensity is located at the inboard side, that extends from the lower to upper channels of the viewing area of AXUVD, while in the case of sustained detachment with the island (right figure) the peak radiation moves to the bottom part which corresponds to the viewing line of around ch.4 of AXUVD, being consistent with the experimental observations. The difference is considered to come from the Te modulation introduced by the  $n/m=1/1$  island which prevents strong carbon radiation inside the island with the robust Te flattening with  $> 10$  eV and thus the radiation tends to localize at the opposite side to the O-point, i.e. X-point. Signature of selective cooling at the X-point is also observed in the divertor probe measurements. Fig.9 shows temporal evolutions of ion saturation currents at two different divertor plates, inboard & upper divertor plates, which connect to the flux tubes around O- and X-point of the island respectively in the case with the  $n/m=1/1$  perturbation. In the case without the island the particle flux to the inboard divertor saturates first around  $t=2.4$  s showing small oscillation, and around  $t=2.8$  s the both inboard & upper divertor flux start to decrease in almost same time scale leading to radiative collapse. In the case with the island, on the other hand, the particle flux from the X-point flux tube starts to decrease around  $t=2.6$  s while those from O-point still continues to increase and the roll over starts about 0.15 second later, around  $t=2.75$  s. Such behavior is always observed with the sustained detachment case with the island and this indicates that the X-point flux tubes are selectively cooled down first with the  $n/m=1/1$  island at the detachment transition resulting in the slightly earlier detachment onset there. The results obtained from these diagnostics, Thomson scattering, AXUVD and the divertor probes as well as from the 3D simulations are consistent each other indicating that the Te modulation introduced by the  $n/m=1/1$  island significantly affects the radiation distribution which seems to localize around X-point.

## V. EFFECTS OF ISLAND SIZE AND RADIAL LOCATION ON THE DETACHMENT STABILIZATION

The perturbation coil current ( $I_{\text{coil}}$ ) was varied to see the effect of the island size on the detachment stabilization. The plasma response to the perturbation field was monitored by saddle loop coils and it is found that the behavior changes depending on the perturbation strength (coil currents) and not straightforward. But at least it is confirmed that the island is not healed during the detachment phase or even found to be slightly enlarged. The plasma response during the attach/detachment phase will be reported in a separated paper. Plotted in Fig.10 is the detachment transition densities,  $n_{\text{detach}}$ , as well as the radiative collapse densities,  $n_{\text{collapse}}$ , as a function of  $I_{\text{coil}}$ . The radiative collapse density is defined as the density at which the stored energy starts to roll over just before the collapse during the density ramp up. The island size estimated from the  $T_e$  flattening at the attachment phase is about 0.15 m with the full perturbation current of 3400A as shown in Fig.7 (c). It is found that  $n_{\text{collapse}}$  is almost independent of the perturbation currents being estimated at  $8$  to  $9 \times 10^{19} \text{ m}^{-3}$ , while  $n_{\text{detach}}$  increases with decreasing perturbation current and around 1500A it seems to approach  $n_{\text{collapse}}$ . The sustained detachment was realized only at  $I_{\text{coil}} > 1900\text{A}$  and below this value it was difficult to control the density after detachment and the plasma easily went to radiative collapse. The evolution of radiation intensity during density ramp up is depicted in Fig.11 in more detail, where the radiation measured by the resistive bolometer is plotted as a function of line averaged density for different perturbation current  $I_{\text{coil}}$ 's. Up to  $4 \times 10^{19} \text{ m}^{-3}$  there is no significant difference in the radiation intensity for the different  $I_{\text{coil}}$ 's, but at  $> 4 \times 10^{19} \text{ m}^{-3}$  it is seen that the larger perturbation field gives rise to higher radiation power which results in the lower detachment transition density as seen in Fig.10 too. Also it is noted that after the detachment transition the radiation intensity becomes less sensitive to the density as shown in the figure, and that the detached plasma is fed with reduced but substantial amount of gas puff as shown in Fig.3 (g). This gives us easy control of the detached plasma and also reattachment was readily achieved by reducing the gas puff rate, which is not shown here though. At  $I_{\text{coil}}=1900\text{A}$  the density could be even increased slightly above the  $n_{\text{collapse}}$  once the discharge entered the sustained detachment operations. It implies that the operational density range depends also on the history of ramp up or operation mode, not only on the absolute density. With decreasing  $I_{\text{coil}}$  the detachment transition density gradually increases and finally at 1500A the detachment phase could not be sustained as shown in the figure. The behavior is very similar to that without island ( $I_{\text{coil}}=0\text{A}$ ) where the radiation intensity is very sensitive to the density after the detachment transition and it is very difficult to sustain the detachment phase. Such the geometrical effect of the island width has been investigated in the island divertor configuration in W7-AS, where the larger island was found to provide a stable detachment operation [14] and the effect of coupling between core and edge plasma through the neutral penetration inside LCFS was discussed based on the 3D transport simulation with EMC3-EIRENE [15].

The radial location of the island is also found to be important factor to realize the sustained

detachment. When the island location is shifted radially inward by changing iota profile, it becomes difficult to control the detachment. Fig.12 shows the radial profiles of  $T_e$  during the attachment phase as visualization of the island location together with the LCFS which is estimated in the configurations without the islands. For the two cases with island indicated with closed and open circles the detachment was successfully sustained, while for the case represented with triangles the density ramp up simply led to radiative collapse. It seems that in order to realize the sustained detachment the island should be located radially outer enough, probably outside of LCFS, in which case the island flux tubes interact with the stochastic field lines in the edge region. The absolute  $T_e$  values at the islands, which are slightly less than 100 eV for the sustained detachment case and nearly 200 eV for the radiative collapse case, might also play an important role to affect the radiation pattern of carbon whose radiative power loss rate coefficient,  $L(T_e)$ , has strongly nonlinear dependence on  $T_e$  especially below 100 eV.

## VI. DIVERTOR PARTICLE FLUX BEHAVIOR DURING DETACHMENT

Fig.13 shows the particle flux profile at the inboard divertor plates together with the connection length with black line (shot number : 85946). Since the most of the plasma is carried by the long connection length flux tubes that usually penetrate deep into the stochastic SOL, a peak of the particle flux is correlated with the long connection length. The left and right sides of the figure correspond to the private and SOL region, respectively. At the attachment phase, the particle flux decays very quickly towards the both sides, as shown in the figure, by an order of magnitude in  $\sim 1$  cm. This quick decay is understood as being due to the very short connection length (several meters) flux tubes adjacent to the peak of the long flux tubes, which travel only less than half torus without penetrate to the stochastic SOL. At the detachment phase, the peak value and the flux at the SOL side decrease almost one order of magnitude, while into the private region there observed remarkable flux broadening, which compensates the reduction at the peak value partly and the resulting total flux reduction summed over the probe arrays becomes a factor of 3, as seen in Fig.3 (b). Such flux broadening is also clearly detected at the probes installed at the outboard side private region, as shown in Fig.14 where the time traces of ion saturation current of the private probes are plotted with different colors indicating different toroidal sections (shot number : 93210). At the almost all toroidal sections, the flux increases as the plasma detaches from the divertor plates, accompanied by the intermittent plasma ejections of 50 to 60 Hz as shown in the expanded view in Fig.14, where the flux at the strike point is also plotted for comparison. The ejections are observed also at the strike point flux at the almost same timings as those at the private region. Plotted in Fig.15 are fluctuation intensity of the private particle flux at the detachment phase (averaged over

$t=2.5\sim 3.3$  s),  $\sqrt{(I_{is,detach} - \bar{I}_{is,detach})^2} / \bar{I}_{is,detach}$ , where  $\bar{I}_{is,detach}$  is the time averaged value, as well

as the averaged private flux at the detachment phase normalized with those just before the detachment transition (averaged over  $t=2.0\sim 2.1$  s),  $\bar{I}_{is,detach} / \bar{I}_{is,attach}$ , as a function of toroidal angle. It is clearly seen that the both fluctuation and the averaged flux have  $n=1$  mode structure, although their peak locations are slightly different each others, i.e. fluctuation at  $\phi = 126 \sim 162$  deg. while the averaged value at  $\phi = 90$  deg., respectively. The profiles might reflect the  $n/m=1/1$  island structure, the O-region of which is located at outboard side of  $\phi=162$  deg. On the other hand, the flux broadening to the private region has not been observed at the upper divertor probes, where simply the ion saturation current decreases at all the probe tips. Although the absolute value of the particle flux at the private region is smaller than those at the strike points by three orders of magnitude as shown in the figure, the area of private region is estimated as being larger than the strike points by two orders of magnitude. It means that at the detachment phase the contribution of private flux can be about 10 % of total flux. This might change the recycling pattern during the detachment phase, and indeed such signature is observed in the neutral pressure distribution as shown in Fig.16 (shot number : 93210), where the outboard neutral pressure increases at the detachment phase while the upper divertor pressure decreases. The change of the recycling pattern can affect the detachment stability by changing radiation pattern through the density profile that is largely determined by ionization distribution, as also discussed in ref.[31]. The effect of the recycling pattern on the detachment stability is under investigation. The temporal evolution of inboard and lower divertor pressure is not straightforward, the reason of which is not yet identified. However, the neutral pressure at the divertor region is found to be kept at substantially high level during the detachment at all locations. The high neutral flux can provide efficient divertor pumping capability being compatible with the reduction of power load at the divertor plate as observed in Fig.3 (d).

## VII. SUMMARY AND DISCUSSION

It is found that the remnant island structure of  $n/m=1/1$  mode created in the stochastic magnetic boundary has stabilizing effect on the radiation region at the detached divertor operation with the core plasma being unperturbed. The reduction of divertor power load is estimated by a factor of 3 ~ 10 from the divertor probes. The radiation profile measurements indicate that the radiation peak is located around X-point of the remnant island, far outside of LCFS. This is consistent with the divertor probe signals which show signature of selective cooling of X-point flux tubes just before the detachment transition. The Te profile obtained by the Thomson scattering system exhibits clear flattening inside the island which is maintained throughout the detachment phase with more than 10 eV. Taking into account the radiative power loss coefficient of carbon L(Te), which has strong

nonlinearity below 10 eV, such the temperature modulation affects the radiation pattern, i.e. less radiation inside the island while X-point being expected to radiate more due to the lower  $T_e$ . This picture is also supported by the EMC3-EIRENE simulations which shows localization of radiation around X-point. The computational time for this detachment transition, however, becomes lengthy due to the strong nonlinearity of the atomic/molecular process which requires many iteration until convergence. Although further increase of density is necessary to analyze the later phase of detachment as mentioned in section IV, it already gives us enough information to interpret the experimental results.

The divertor plasma temperature estimated from the probe array shows rather large scatter during the detachment. This is due to the very low temperature and also to the oscillation of the divertor flux during the detachment. This prevents us from accurately estimating the power balance in comparison with the radiation measurements. But since the AXUVD indicates about factor of 3 increase of radiation at the detachment transition (Fig.3 (e)) and about factor of 2 by the resistive bolometer (Fig.11), the reduction of divertor power flux is roughly consistent with the radiation within the scattered range, assuming toroidal uniformity of the detachment. The signature of volume recombination observed by the spectroscopy throughout the torus supports this assumption. Absolute calibration as well as toroidal profile of the radiation power and the divertor power flux measurements is under improvement.

One of the reasons for the intermittent oscillation of divertor flux might be attributed to the high sensitivity (nonlinearity) of radiation function or ionization rate coefficient of impurity/hydrogen to the temperature at the cold plasma below 10 eV, where any small fluctuations in the plasma parameters would be amplified via transition between multiple equilibrium states in the system. The computation with EMC3-EIRENE also shows such oscillation during the iterations. Other than this, there are several possibilities to excite oscillation near density limit as discussed in ref.[32]. The cause of oscillation is under investigation.

The stability of the detachment control is clearly illustrated in Fig.10 and 11, where the radiation intensity is shown to become relatively insensitive to the density after the detachment transition with the application of the perturbation field. Also it is noted that the detached plasma is sustained with finite gas puff as shown in Fig.3 (g), so that the reattachment was easily done by reducing the gas puff rate. These features provide us controllability to maintain the radiative plasma within a certain range of operation density. Otherwise it is very difficult to stop the plasma collapse as soon as the detachment onsets as shown in the case without the island or with smaller perturbation field. The similar feature of the detachment stability in terms of the island size was observed in ref. [14, 15]. The effect of the neutral penetration inside LCFS as proposed as a controlling term of the stability is being analyzed in the present cases. The stability of the detachment might also be affected by the recycling pattern [31], which is indeed found to be coupled with the island structure as shown

in Fig.15. Understanding the mechanism of the detachment stabilization with the remnant island in the stochastic magnetic boundary remains future work.

The data presented here, also together with the analyses in W7-AS, indicate a possibility to control divertor detachment by edge magnetic field geometry, which in turn contributes to divertor design of the helical devices as well as of the non-axisymmetric tokamaks such as those with resonant magnetic perturbation field.

#### ACKNOWLEDGEMENTS

The authors are grateful for the support for the computational resources: Plasma Simulator SR16000 L2 powered by HITACHI Ltd, and AMD Opteron-InfiniBand Cluster Machine, by Grant-in-Aid for Science Research on Priority Areas (Area 465, No.18070005) from Ministry of Education, Culture, Sports, Science and Technology, Japan. The part of the computational work is also financially supported by the budget code NIFS09ULPP538.

#### REFERENCES

- [1] G.F. Matthews, *J. Nucl. Mater.* **220-222**, 104 (1995).
- [2] C.S. Pitcher and P.C. Stangeby, *Plasma Phys. Control. Fusion* **39**, 779 (1997).
- [3] O. Gruber, A. Kallenbach, M. Kaufmann, K. Lackner, V. Mertens, J. Neuhauser, F. Ryter, H. Zohm, M. Bessenrodt-Weberpals, K. Buechl et al., *Phys. Rev. Lett.* **74**, 4217 (1995).
- [4] J. Neuhauser, M. Alexander, G. Becker, H-S. Bosch, K. Buechl, D. Coster, R. Dux, A. Field, S. Fiedler, Ch. Fuchs et al., *Plasma Phys. Control. Fusion* **37**, A37 (1995).
- [5] B. Lipschultz, J. Goetz, B. LaBombard, G.M. McCracken, J.L. Terry, M. Graf, R.S. Granetz, D. Jablonski, C. Kurz, A. Niemczewski, J. Snipes, *J. Nucl. Mater.* **220-222**, 50 (1995).
- [6] N. Asakura, H. Hosogane, S. Tsuji-IIO, K. Itami, K. Shimizu, M. Shimada, *Nucl. Fusion* **36**, 795 (1996).
- [7] A. Loarte, R.D. Monk, J.R. Martin-Solis, D.J. Campbell, A.V. Chankin, S. Clement, S.J. Davies, J. Ehrenberg, S.K. Erents, H.Y. Guo et al., *Nucl. Fusion* **38**, 331 (1998).
- [8] M.E. Fenstermacher, S.L. Allen, N.H. Brooks, D.A. Buchenauer, T.N. Carlstrom, J.W. Cuthbertson, E.J. Doyle, T.E. Evans, P.-M. Garbet, R.W. Harvey et al., *Phys. Plasmas* **4**, 1761 (1997).
- [9] S. Konoshima, H. Tamai, Y. Miura, S. Higashijima, H. Kubo, S. Sakurai, K. Shimizu, T. Takizuka, Y. Koide, T. Hatae, H. Takenaga, *J. Nucl. Mater.* **313-316**, 888 (2003).
- [10] A. Komori, H. Yamada, S. Sakakibara, O. Kaneko, K. Kawahata, T. Mutoh, N. Ohya, S. Imagawa, K. Ida, Y. Nagayama et al., *Nucl. Fusion* **49**, 104015 (2009).

- [11] P. Grigull, K. McCormick, J. Baldzuhn, R. Burhenn, R. Brakel, H. Ehmler, Y. Feng, F. Gadelmeier, L. Giannone, D. Hartmann et al., *Plasma Phys. Control. Fusion* **43**, A175 (2001).
- [12] B.J. Peterson, J. Miyazawa, K. Nishimura, S. Masuzaki, Y. Nagayama, N. Ohyaabu, H. Yamada, K. Yamazaki, T. Kato, I. Murakami et al., *Plasma and Fusion Research* **1**, 045 (2006).
- [13] J. Miyazawa, S. Masuzaki, M. Goto, N. Tamura, R. Sakamoto, B.J. Peterson, I. Yamada, K. Narihara, K. Tanaka, T. Tokuzawa et al., *Plasma and Fusion Research* **1**, 026 (2006).
- [14] P. Grigull, K. McCormick, Y. Feng, A. Werner, R. Brakel, H. Ehmler, F. Gadelmeier, D. Hartmann, D. Hildebrandt, R. Jaenicke et al., *J. Nucl. Mater.* **313-316**, 1287 (2003).
- [15] Y. Feng, F. Sardei, J. Kisslinger, P. Grigull, K. McCormick, D. Reiter, L. Giannone, R. Koenig, N. Ramasubramanian, H. Thomsen and U. Wenzel, *Nucl. Fusion* **45**, 89 (2005).
- [16] Y. Feng, F. Sardei, J. Kisslinger, P. Grigull, K. McCormick and D. Reiter, *Contributions to Plasma Physics*, **44**, 57 (2004).
- [17] D. Reiter, M. Baelmans and P. Boerner, *Fusion Sci. Technol.*, **47** 172 (2005). ; <http://www.eirene.de/>
- [18] Ph. Ghendrih et al., *J. Nucl. Mater.* **266-269** (1999) 189.
- [19] K.H. Finken, S.S. Abdullaev, A. Kaleck and G.H. Wolf, *Nucl. Fusion* **39**, 637 (1999).
- [20] T. Evans, R. Moyer, K. Burrell, M. Fenstermacher, I. Joseph, A. Leonard, T. Osborne, G. Porter, M.J. Schaffer, P. Snyder et al., *Nature Phys.* **2**, 419 (2006).
- [21] Y. Liang, H.R. Koslowski, P.R. Thomas, E. Nardon, B. Alper, P. Andrew, Y. Andrew, G. Arnoux, Y. Baranov, M. Becoulet et al., *Phys. Rev. Lett.* **98**, 265004 (2007).
- [22] N. Ohyaabu, T. Watanabe, H. Ji, K. Yamazaki, K. Akaishi, N. Inoue, A. Komori et al., *Nucl. Fusion*, **34**, 387 (1994).
- [23] F. Nguyen, P. Ghendrih, A. Grosman, *Nucl. Fusion*, **37**, 743 (1997).
- [24] S. Masuzaki, T. Morisaki, N. Ohyaabu, A. Komori, H. Suzuki, N. Noda, Y. Kubota, R. Sakamoto, K. Narihara, K. Kawahata et al., *Nucl. Fusion* **42**, 750 (2002).
- [25] M. Kobayashi, Y. Feng, S. Masuzaki, M. Shoji, J. Miyazawa, T. Morisaki, N. Ohyaabu, N. Ashikawa, A. Komori, O. Motojima et al., *J. Nucl. Mater.*, **363-365**, 294 (2007).
- [26] Y. Feng, M. Kobayashi, T. Morisaki, S. Masuzaki, J. Miyazawa, B.J. Peterson, S. Morita, M. Shoji, K. Ida, I. Yamada et al., *Nucl. Fusion* **48**, 024012 (2008).
- [27] M. Kobayashi, Y. Feng, S. Morita, S. Masuzaki, N. Ezumi, T. Kobayashi, M.B. Chowdhuri, H. Yamada, T. Morisaki, N. Ohyaabu et al., "Transport characteristics in the stochastic magnetic boundary of LHD : Magnetic topology and its impact on divertor physics and impurity transport", accepted for publication in *Fusion Science and technology*.
- [28] Y. Corre, J. Gunn, B. Pegourie, R. Guirlet, C. DeMichelis, R. Giannella, P. Ghendrih, J. Hogan, P. Monier-Garbet, A. Azeroual et al., *Nucl. Fusion* **47**, 119 (2007).
- [29] G. Telesca, E. Delabie, O. Schmitz, S. Brezinsek, K.H. Finken, M.von Hellermann, M.

- Jakubowski, M. Lehnen, Y. Liang, A. Pospieszczyk et al., J. Nucl. Mater. **390-391**, 227 (2009).
- [30] M. Kobayashi, Y. Feng, S. Morita, M.B. Chowdhuri, M. Goto, S. Masuzaki, N. Ohya, T. Morisaki, H. Yamada, I. Yamada et al., J. Nucl. Mater., **390-391**, 325 (2009).
- [31] M.Z. Tokar J. Rapp, D. Reiser, U. Samm, F.C. Schueller, G. Sergienko, P.C. de Vries et al., J. Nucl. Mater. **266-269**, 958 (1999).
- [32] K. Itoh, S.I. Itoh and L. Giannone, J. Phys. Soc. Jpn. **70**, 3274 (2001).

## FIGURE CAPTIONS

Fig.1 (Color online) (a) Structure of the superconducting helical coils, perturbation coils and the plasma shape. LHD is a heliotron type device with poloidal winding number of  $l=2$  and toroidal field periods of  $n=10$ . Major radius = 3.90 m, averaged minor radius  $\sim 0.70$  m. (b) Inside view of LHD. The divertor plates are installed in-between the helical coils, made of graphite. The first wall is made of stainless steel.

Fig.2 (Color online) Connection length ( $L_C$ ) distribution in poloidal cross section at horizontally elongated section. Upper: without perturbation field. Lower : with the  $n/m=1/1$  resonant magnetic perturbation field. The inner part with long field lines (yellow, red) is called stochastic region, the outer part with mixture of long (yellow, red) and short (blue) is called edge surface layers. The perturbation field creates remnant island in the stochastic region with the O-point located at outboard side in this section. The divertor legs are stretched from the in- and out-board sides towards target plates, which are not shown.

Fig.3 (Color online) Time traces of various plasma parameters at the sustained detachment shot with  $n/m=1/1$  island. (a) line averaged density, (b) divertor particle flux at upper & inboard divertor plates, which are separated toroidally by  $\sim 160$  degrees. (c) electron density (closed circles) and temperature (open squares) at the inboard divertor measured by the Langmuir probe, (d) power flux to inboard divertor plates estimated from the Langmuir probe, (e) radiation intensity measured by AXUVD (solid line) and line emission of  $H_\alpha$  (broken line), (f) stored energy measured by the diamagnetic probe, (g) net NBI heating (solid line) and gas puff rate (broken line), (h) ratio of  $H_\gamma$  to  $H_\beta$  measured by the visible spectroscopy at different toroidal locations indicated by toroidal angle, respectively. The detachment occurs at  $t \sim 2.9$  s and was sustained until the end of discharge terminated by stop of NBI heating. (#85946)

Fig.4 (Color online) Radial profiles of (a) electron temperature ( $T_e$ ), (b) electron density ( $n_e$ ), (c) electron pressure ( $T_e n_e$ ), obtained by the Thomson scattering system, at attachment ( $t=2.80$  s) and detachment ( $t=4.00$  s) phases. (#85946)

Fig.5 (Color online) Iron emission measured by the VUV spectroscopy for different densities,  $2.0 \times 10^{19} \text{ m}^{-3}$  with attached plasma (black),  $4.0 \times 10^{19} \text{ m}^{-3}$  with attached plasma (blue) and  $6.6 \times 10^{19} \text{ m}^{-3}$  with detached plasma (red), respectively. The wave length of each line is indicated in the figure in angstrom. The line emissions are significantly suppressed at high density considered due to the impurity screening effect in the stochastic magnetic field. This effect is also available during the

detachment phase.

Fig.6 (Color online) Time traces of (a) line averaged density, (b) radiation intensity measured by AXUVD, (c) divertor particle flux, (d) gas puff rate, respectively. Thin (blue) lines : sustained detach with  $n/m=1/1$  island, thick (red) lines : radiative collapse without the island. (#85946 for with island, #85948 for without island).

Fig.7 (Color online) Radial profiles of  $T_e$  and  $n_e$  at the edge region for (a) & (b) without the island, where the plasma goes to radiative collapse at  $t \sim 4.0$ s, (c) & (d) with the island where the sustained detachment was realized at  $t > 2.900$  s. The latter case is characterized by the  $T_e$  flattening inside the island with  $> 10$  eV. LCFS is located around  $R=4.55$  m. The dense ( $\sim 10^{20} \text{ m}^{-3}$ ) and cold (a few eV) plasma is formed outside the LCFS. (#85946 for with island, #85948 for without island).

Fig.8 (Color) (a) Temporal evolution of line integrated radiation profiles measured by the AXUVD for without (left figure) & with (right figure) the  $n/m=1/1$  island. (b) The viewing lines of the AXUVD, which has 16 channels numbered from the lower to upper lines. (c) Initial results of impurity radiation distributions obtained with EMC3-EIRENE for without (left figure) & with (right figure) the island. The densities at the LCFS are  $7.0 \times 10^{19} \text{ m}^{-3}$  (without island, left) &  $6.5 \times 10^{19} \text{ m}^{-3}$  (with island, right), respectively. These conditions correspond to  $t \sim 3.0$  &  $3.1$  s for without & with island, respectively. The island O-point is located at the top of the plasma in this cross section as indicated in the right figure in (c). (#85946 for with island, #85948 for without island).

Fig.9 Temporal evolution of the ion saturation currents measured at the upper (grey lines) & inboard (black lines) divertor plates. (a) without the  $n/m=1/1$  island, (b) with the island. In the case with the island, the upper & inboard divertor probes are connected to the flux tubes around X- & O-point of the island, respectively. The X-point particle flux rolls over earlier than those of O-point in (b), indicating selective cooling of X-point flux tubes. (#93204 for with island, #93207 for without island).

Fig.10 Radiative collapse density,  $n_{\text{collapse}}$  (triangles), and detachment transition density,  $n_{\text{detach}}$  (open circles), as a function of the  $n/m=1/1$  perturbation coil current,  $I_{\text{coil}}$ . The island size at the full current of 3400A is about 0.15 m (Fig.7 (c)). The sustained detachment was realized only with  $I_{\text{coil}} > 1900$ A.  $n_{\text{collapse}}$  is almost independent of  $I_{\text{coil}}$ .

Fig.11 (Color online) Evolution of radiation intensity measured by the resistive bolometer as a function of line averaged density, for different  $n/m=1/1$  perturbation current,  $I_{\text{coil}}$  : closed

circles=3400A, open circles=3000A, triangles=2500A, diamonds=1900A, squares=1500A, crosses=0A. At the sustained detachment phase, the radiation intensity becomes less sensitive to the density change and while the plasma is sustained with residual gas puff, providing easy control of the detached plasma.

Fig.12 Te profiles during attachment phase as visualization of island location for three different configurations. The location of LCFS is estimated for the configuration without the islands. The radial extent of the island in the each configuration is indicated with the horizontal bar. The sustained detachment was realized only for the configurations with closed and open circles.

Fig.13 Divertor particle flux profiles at the attachment (closed circles,  $t=2.800$  s) and detachment (open circles,  $t=4.000$  s) phase at the inboard divertor plates. The connection length ( $L_C$ ) is indicated with solid lines. The left and right sides of the figure correspond to the private and SOL region, respectively. There appears flux broadening to the private region during the detachment phase. (#85946)

Fig.14 (Color online) Time traces of particle flux in the private region of outboard divertor plates. The different colors indicate different toroidal locations in degree. Shown in the expanded view are one of the private particle flux traces at toroidal angle of 162 degree (green) and that of strike point at inboard divertor (grey). The detachment occurs at  $t=2.1$  s. (#93210)

Fig.15 Toroidal profiles of fluctuation intensity of particle flux in the private region during detachment (open circles, left axis),  $\sqrt{(I_{is,detach} - \bar{I}_{is,detach})^2} / \bar{I}_{is,detach}$ , and the time averaged particle flux in the private region during the detachment normalized with the value just before the detachment transition (triangles, right axis),  $\bar{I}_{is,detach} / \bar{I}_{is,attach}$ . The fluctuation is averaged over  $t=2.5\sim 3.3$  s.  $\bar{I}_{is,attach}$  is averaged over  $t=2.0\sim 2.1$  s. There appears clear  $n=1$  mode structure in the both profiles. (#93210)

Fig.16 Temporal evolution of neutral pressure measured at inboard (grey line), outboard (solid line with crosses), upper (dashed line) and lower (solid line) divertors. The detachment transition occurs at  $t=2.1$  s. The outboard pressure increase while upper divertor pressure decrease, which might reflect the change of recycling pattern caused by the private particle flux during detachment as shown in Fig.13-15. The behavior of inboard and lower divertor pressure is not straightforward. (#93210)

Fig.1 M.Kobayashi et al.

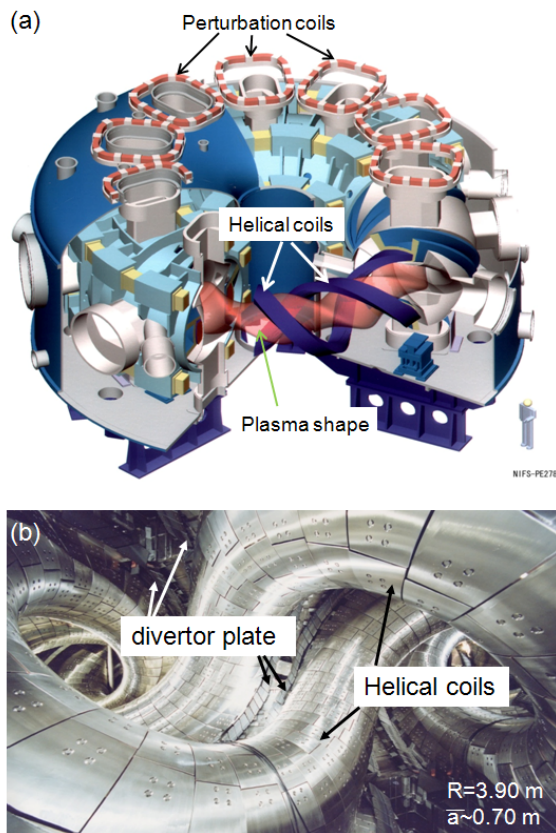


Fig.1 (Color online) (a) Structure of the superconducting helical coils, perturbation coils and the plasma shape. LHD is a heliotron type device with poloidal winding number of  $l=2$  and toroidal field periods of  $n=10$ . Major radius = 3.90 m, averaged minor radius  $\sim 0.70$  m. (b) Inside view of LHD. The divertor plates are installed in-between the helical coils, made of graphite. The first wall is made of stainless steel.

Fig.2 M.Kobayashi et al.

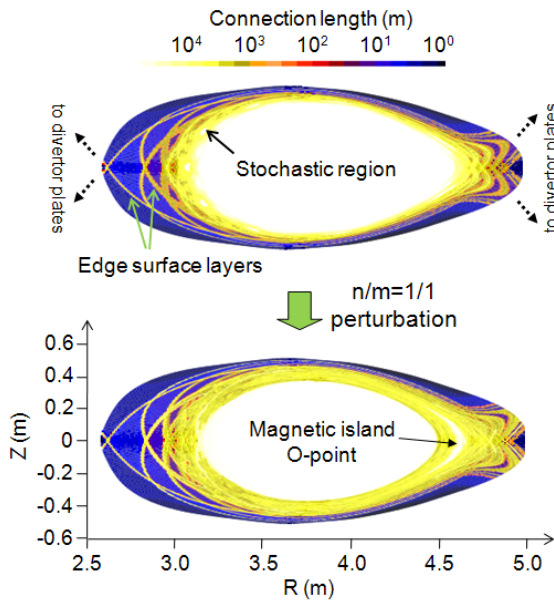


Fig.2 (Color online) Connection length ( $L_C$ ) distribution in poloidal cross section at horizontally elongated section. Upper: without perturbation field. Lower : with the  $n/m=1/1$  resonant magnetic perturbation field. The inner part with long field lines (yellow, red) is called stochastic region, the outer part with mixture of long (yellow, red) and short (blue) is called edge surface layers. The perturbation field creates remnant island in the stochastic region with the O-point located at outboard side in this section. The divertor legs are stretched from the in- and out-board sides towards target plates, which are not shown.

Fig.3 M.Kobayashi et al.

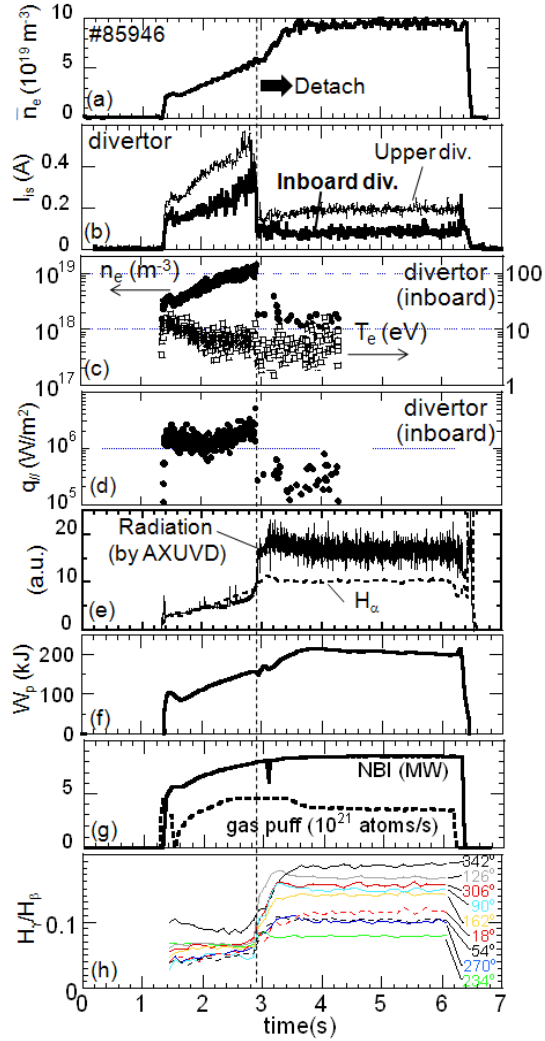


Fig.3 (Color online) Time traces of various plasma parameters at the sustained detachment shot with  $n/m=1/1$  island. (a) line averaged density, (b) divertor particle flux at upper & inboard divertor plates, which are separated toroidally by  $\sim 160$  degrees. (c) electron density (closed circles) and temperature (open squares) at the inboard divertor measured by the Langmuir probe, (d) power flux to inboard divertor plates estimated from the Langmuir probe, (e) radiation intensity measured by AXUVD (solid line) and line emission of  $H_\alpha$  (broken line), (f) stored energy measured by the diamagnetic probe, (g) net NBI heating (solid line) and gas puff rate (broken line), (h) ratio of  $H_\gamma$  to  $H_\beta$  measured by the visible spectroscopy at different toroidal locations indicated by toroidal angle, respectively. The detachment occurs at  $t \sim 2.9$  s and was sustained until the end of discharge terminated by stop of NBI heating. (#85946)

Fig.4 M.Kobayashi et al.

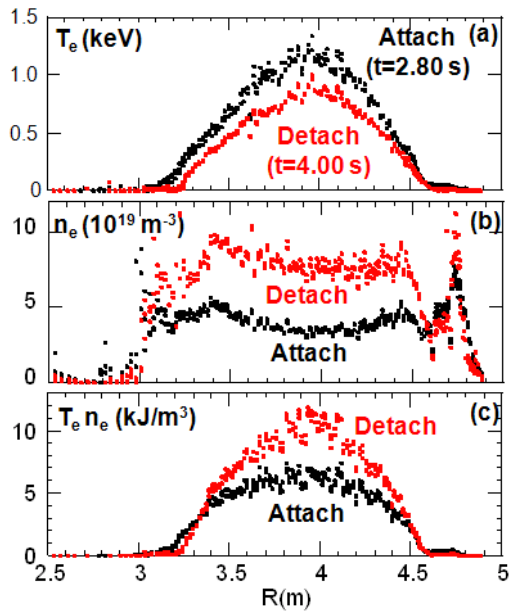


Fig.4 (Color online) Radial profiles of (a) electron temperature ( $T_e$ ), (b) electron density ( $n_e$ ), (c) electron pressure ( $T_e n_e$ ), obtained by the Thomson scattering system, at attachment ( $t=2.80$  s) and detachment ( $t=4.00$  s) phases. (#85946)

Fig.5 M.Kobayashi et al.

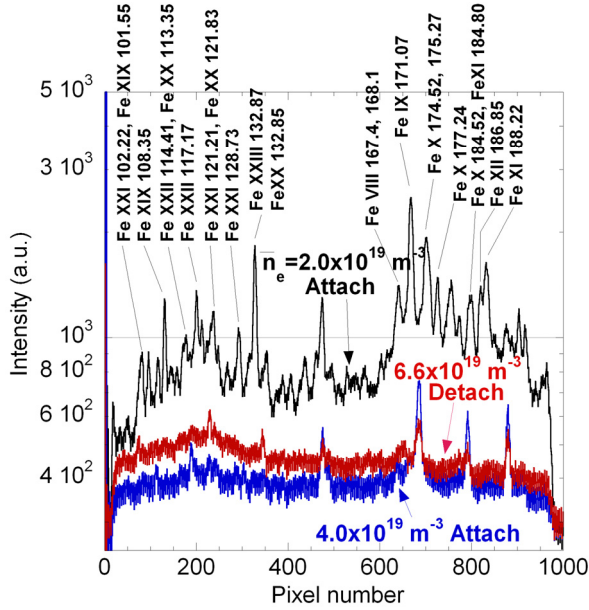


Fig.5 (Color online) Iron emission measured by the VUV spectroscopy for different densities,  $2.0 \times 10^{19} \text{ m}^{-3}$  with attached plasma (black),  $4.0 \times 10^{19} \text{ m}^{-3}$  with attached plasma (blue) and  $6.6 \times 10^{19} \text{ m}^{-3}$  with detached plasma (red), respectively. The wave length of each line is indicated in the figure in angstrom. The line emissions are significantly suppressed at high density considered due to the impurity screening effect in the stochastic magnetic field. This effect is also available during the detachment phase.

Fig.6 M.Kobayashi et al.

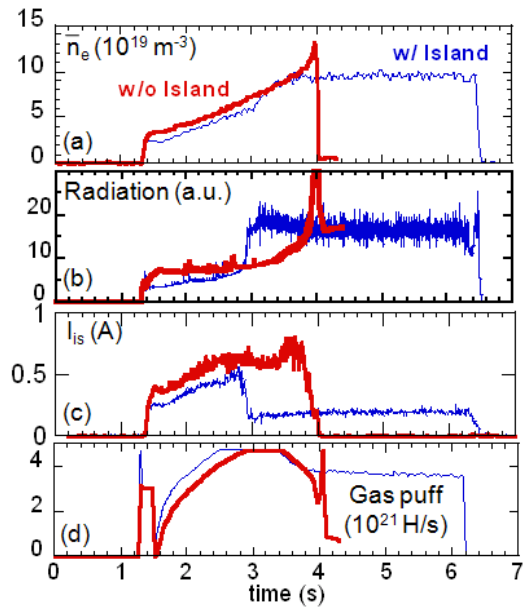


Fig.6 (Color online) Time traces of (a) line averaged density, (b) radiation intensity measured by AXUVD, (c) divertor particle flux, (d) gas puff rate, respectively. Thin (blue) lines : sustained detach with  $n/m=1/1$  island, thick (red) lines : radiative collapse without the island. (#85946 for with island, #85948 for without island).

Fig.7 M.Kobayashi et al.

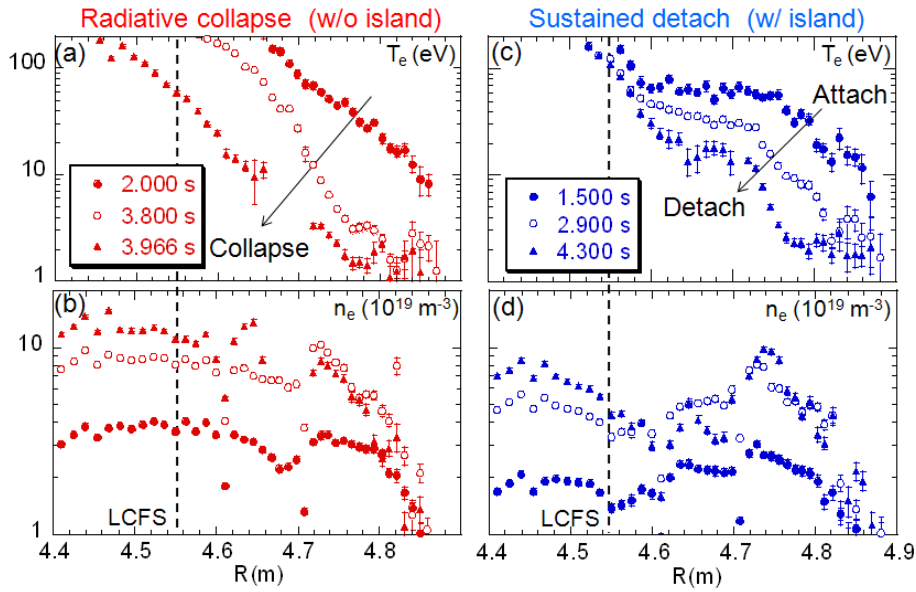


Fig.7 (Color online) Radial profiles of  $T_e$  and  $n_e$  at the edge region for (a) & (b) without the island, where the plasma goes to radiative collapse at  $t \sim 4.0$  s, (c) & (d) with the island where the sustained detachment was realized at  $t > 2.900$  s. The latter case is characterized by the  $T_e$  flattening inside the island with  $> 10$  eV. LCFS is located around  $R=4.55$  m. The dense ( $\sim 10^{20} \text{ m}^{-3}$ ) and cold (a few eV) plasma is formed outside the LCFS. (#85946 for with island, #85948 for without island).

Fig.8 M.Kobayashi et al.

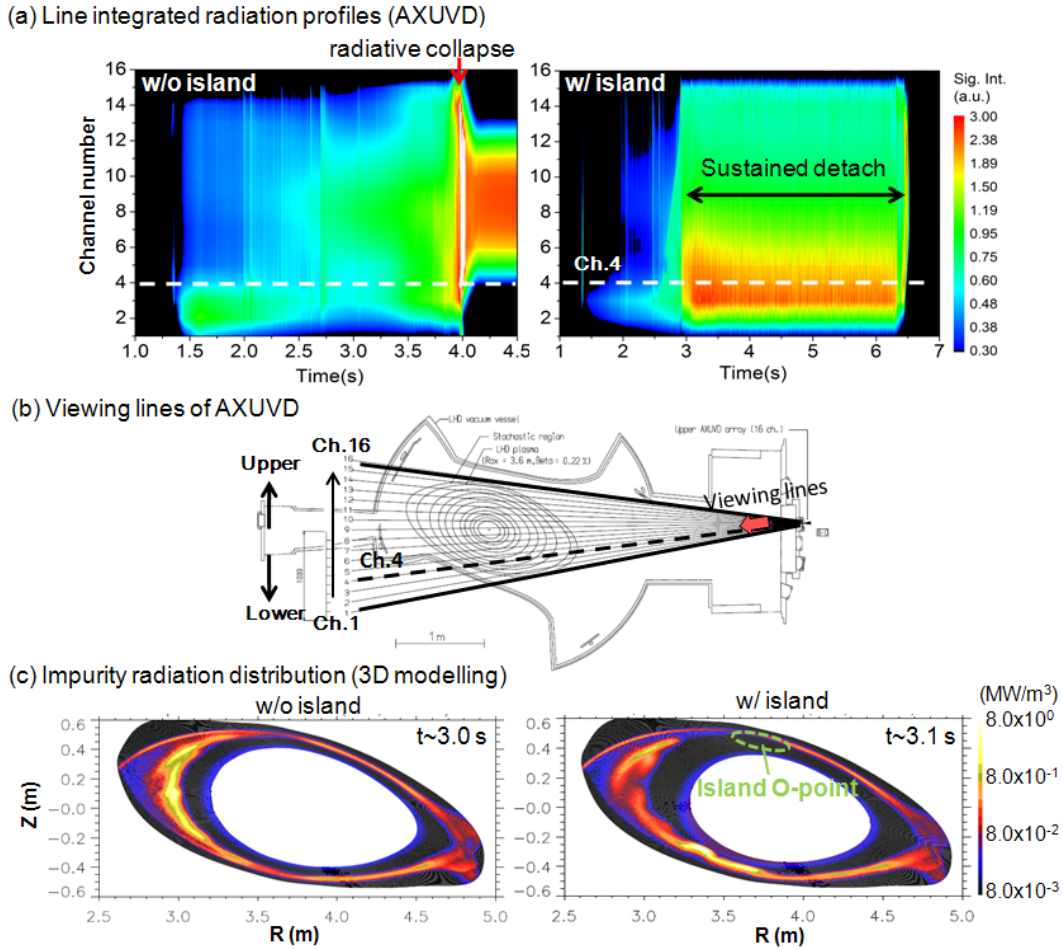


Fig.8 (Color) (a) Temporal evolution of line integrated radiation profiles measured by the AXUVD for without (left figure) & with (right figure) the  $n/m=1/1$  island. (b) The viewing lines of the AXUVD, which has 16 channels numbered from the lower to upper lines. (c) Initial results of impurity radiation distributions obtained with EMC3-EIRENE for without (left figure) & with (right figure) the island. The densities at the LCFS are  $7.0 \times 10^{19} \text{ m}^{-3}$  (without island, left) &  $6.5 \times 10^{19} \text{ m}^{-3}$  (with island, right), respectively. These conditions correspond to  $t \sim 3.0$  &  $3.1$  s for without & with island, respectively. The island O-point is located at the top of the plasma in this cross section as indicated in the right figure in (c). (#85946 for with island, #85948 for without island).

Fig.9 M.Kobayashi et al.

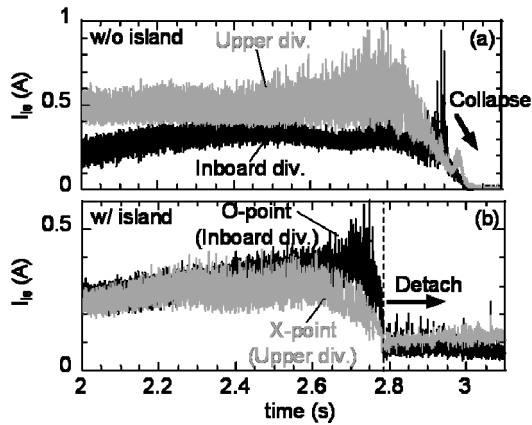


Fig.9 Temporal evolution of the ion saturation currents measured at the upper (grey lines) & inboard (black lines) divertor plates. (a) without the  $n/m=1/1$  island, (b) with the island. In the case with the island, the upper & inboard divertor probes are connected to the flux tubes around X- & O-point of the island, respectively. The X-point particle flux rolls over earlier than those of O-point in (b), indicating selective cooling of X-point flux tubes. (#93204 for with island, #93207 for without island).



Fig.11 M.Kobayashi et al.

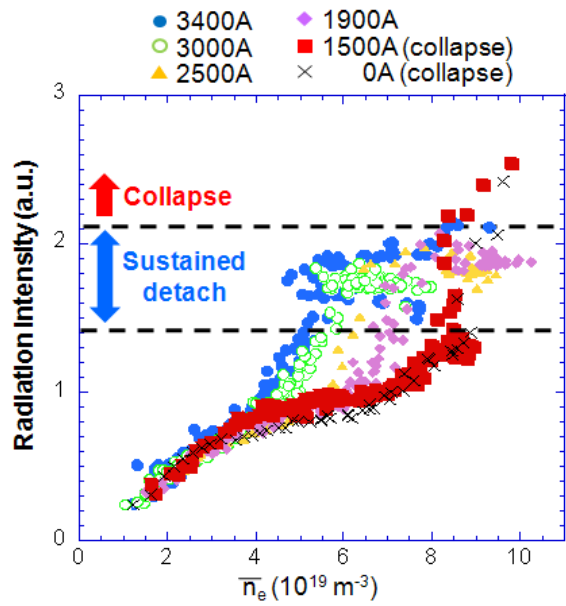


Fig.11 (Color online) Evolution of radiation intensity measured by the resistive bolometer as a function of line averaged density, for different  $n/m=1/1$  perturbation current,  $I_{\text{coil}}$  : closed circles=3400A, open circles=3000A, triangles=2500A, diamonds=1900A, squares=1500A, crosses=0A. At the sustained detachment phase, the radiation intensity becomes less sensitive to the density change and while the plasma is sustained with residual gas puff, providing easy control of the detached plasma.

Fig.12 M.Kobayashi et al.

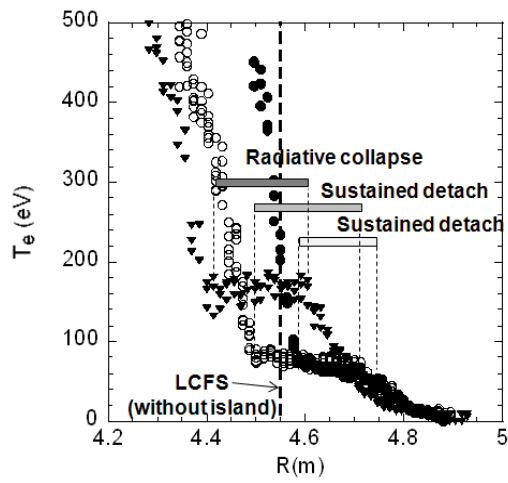


Fig.12  $T_e$  profiles during attachment phase as visualization of island location for three different configurations. The location of LCFS is estimated for the configuration without the islands. The radial extent of the island in the each configuration is indicated with the horizontal bar. The sustained detachment was realized only for the configurations with closed and open circles.

Fig.13 M.Kobayashi et al.

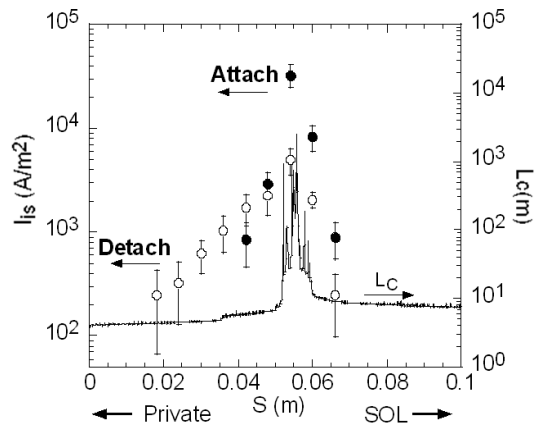


Fig.13 Divertor particle flux profiles at the attachment (closed circles,  $t=2.800$  s) and detachment (open circles,  $t=4.000$  s) phase at the inboard divertor plates. The connection length ( $L_C$ ) is indicated with solid lines. The left and right sides of the figure correspond to the private and SOL region, respectively. There appears flux broadening to the private region during the detachment phase. (#85946)

Fig.14 M.Kobayashi et al.

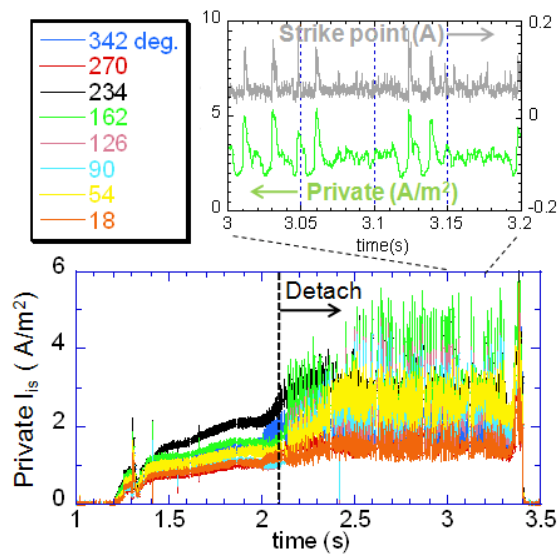


Fig.14 (Color online) Time traces of particle flux in the private region of outboard divertor plates. The different colors indicate different toroidal locations in degree. Shown in the expanded view are one of the private particle flux traces at toroidal angle of 162 degree (green) and that of strike point at inboard divertor (grey). The detachment occurs at t=2.1 s. (#93210)

Fig.15 M.Kobayashi et al.

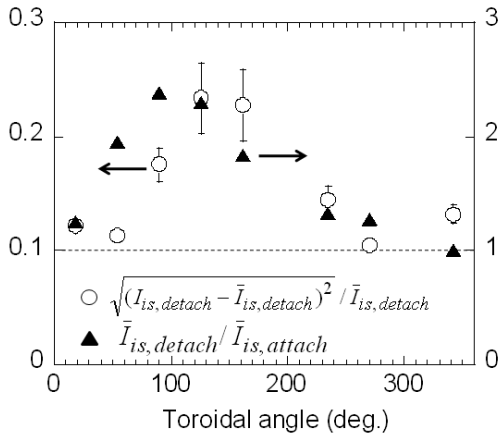


Fig.15 Toroidal profiles of fluctuation intensity of particle flux in the private region during detachment (open circles, left axis),  $\sqrt{(I_{is, detach} - \bar{I}_{is, detach})^2} / \bar{I}_{is, detach}$ , and the time averaged particle flux in the private region during the detachment normalized with the value just before the detachment transition (triangles, right axis),  $\bar{I}_{is, detach} / \bar{I}_{is, attach}$ . The fluctuation is averaged over  $t=2.5\sim 3.3$  s.  $\bar{I}_{is, attach}$  is averaged over  $t=2.0\sim 2.1$  s. There appears clear n=1 mode structure in the both profiles. (#93210)

Fig.16 M.Kobayashi et al.

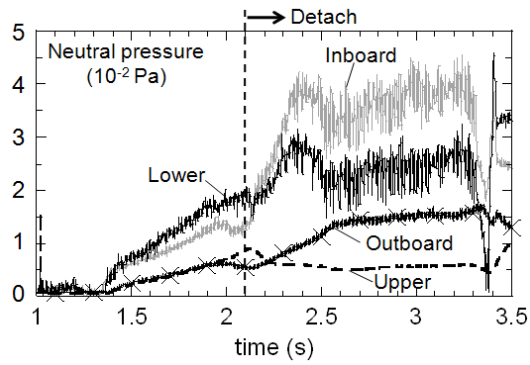


Fig.16 Temporal evolution of neutral pressure measured at inboard (grey line), outboard (solid line with crosses), upper (dashed line) and lower (solid line) divertors. The detachment transition occurs at  $t=2.1$  s. The outboard pressure increase while upper divertor pressure decrease, which might reflect the change of recycling pattern caused by the private particle flux during detachment as shown in Fig.13-15. The behavior of inboard and lower divertor pressure is not straightforward. (#93210)